Earthquake Spectra

RESEARCH PAPER OPEN ACCESS

Near-Source Ground Motion From Normal Faults: Insights From the Physics-Based Numerical Simulations of the 1980 Irpinia Earthquake, Southern Italy

Roberto Paolucci[1] | Chiara Smerzini[1] | Manuela Vanini[1] | Ilario Mazzieri[2] | Victor M. Hernández-Aguirre[3] | Luigi Vadacca[4]

[1]Department of Civil and Environmental Engineering, Politecnico di Milano, Milan, Italy | [2]Department of Mathematics, Politecnico di Milano, Milan, Italy | [3]Earthquake Engineering Research Centre, University of Iceland, Selfoss, Iceland | [4]Ricerca sul Sistema Energetico - RSE S.p.A., Milan, Italy

Correspondence: Chiara Smerzini (chiara.smerzini@polimi.it)

Received: 11 November 2025 | **Revised:** 3 March 2026 | **Accepted:** 8 April 2026

Keywords: Irpinia earthquake | near-source ground motion | physics-based numerical simulations | pulse-like motion | up-dip directivity

ABSTRACT

In this paper, the physics-based numerical simulation of the strongest instrumental earthquake in the recent seismic history of Italy, i.e., the Nov 23, 1980 Irpinia earthquake in Southern Italy, with magnitude M_W 6.8, is presented and discussed. A 3D spectral element model covering an extended region ($147 \times 110\ km^2$) was constructed, with a frequency resolution up to 2 Hz, encompassing a rather complex multi-segment kinematic fault rupture model and a crustal velocity model including the ground topography. Although a strict validation of the numerical model is not possible, owing to the limited data available for this historical earthquake, simulations are found to capture the main features of the spatial and temporal variability of ground motion realistically, as testified by the quantitative comparison with the available recordings and with the macroseismic intensity observations. The results are investigated to gain insights into the key features of near-source ground motion during normal-fault earthquakes, including the spatial variability of the permanent ground deformation field, as well as amplitude, period content, azimuth, and polarization (fault normal vs. fault parallel) of pulse-like signals caused by up-dip directivity effects.

1 | Introduction

Among the various approaches suitable to predict earthquake ground motion, physics-based simulations (PBS) are obtained by numerical integration of the elastodynamic equations within a 3D computational domain embedding the seismic source, the propagation path, and the shallow soil layers. Owing to the expertise gained in recent years (see, e.g., Graves et al. 2011; Paolucci et al. 2018a; McCallen et al. 2021) and to the ever-increasing power of high-performance computing, PBS are becoming a feasible and powerful alternative to empirical approaches for earthquake ground motion assessment. As a matter of fact, although the accuracy of empirical ground motion models (GMM) is

continuously enhanced up to the development of non-ergodic models (Sgobba et al. 2021c; Lavrentiadis et al. 2023) and of sophisticated statistical techniques (e.g. Lanzano et al. 2021; Bortolotti et al. 2024), as more and more records of real earthquakes become available, PBS have the advantage to provide time histories of ground motion accounting for the specific features of the tectonic environment, of the near-source region and/or of the complex geological environment, that may not be sufficiently well sampled yet by available records.

PBS has also attracted interest to simulate earthquake ground motions during historical earthquakes, as in the case of some of the Italian catastrophic events of the past centuries (see, e.g., the 1693 Eastern Sicily, the 1908 Messina Straits, and the 1915 Marsica earthquakes, addressed among others by Munafò et al. 2024, Convertito and Pino 2014, and Paolucci et al. 2016, respectively). First, such simulations may provide useful results for better constraining the seismogenic source of such earthquakes, often hardly known, by exploiting the sparse information available, typically consisting of the macroseismic intensity field and of a few ground motion records, if any. Second, they may provide a comprehensive, realistic picture of the earthquake ground motion, including its near-source features, its attenuation with distance, and its spatial variability at small and large scales. Third, they may better constrain the vulnerability and risk assessment, providing area-specific intensity measures of ground motion either for constructing empirical fragility curves or for generating seismic damage scenarios (Kenawy et al. 2021; Rosti et al. 2023; Miah et al. 2024; Monsalvo-Franco et al. 2025). For these reasons, taking advantage of the large amount of seismic source information and accelerometric records collected after the major Italian earthquakes of the past 20 years, PBS have been extensively used for improving the understanding of earthquake ground motion and of its spatial variability, especially in near-source conditions, such as for L'Aquila 2009 (e.g., Smerzini and Villani 2012; Evangelista et al. 2017; Artale Harris et al. 2025), Po Plain 2012 (e.g., Paolucci et al. 2015) and Central Italy 2016 (e.g., Pitarka et al. 2022; Akinci et al. 2024).

The Irpinia earthquake, which occurred on November 23, 1980, was the last major seismic catastrophe of the past century in Southern Italy, causing about 3000 fatalities. With a moment magnitude M_W of 6.8, it was among the first large earthquakes in the world with a sufficiently extended coverage of analog seismic stations, the recordings of which were used for years as seismic input for earthquake engineering in Italy and Europe, as well as for constraining the empirical GMM at large magnitude. Still, only three stations were lying within less than 15 km distance from the surface projection of the causative fault, so that it was not possible to derive a correlation of the observed largest level of building damage with a well-constrained intensity of shaking. Furthermore, tens of rock and landslides occurred in the near-source area, causing extensive failures in some villages, such as Calitri and Senerchia (Bernard and Zollo 1989; Porfido et al. 2007). Additionally, large ground deformations were observed, sometimes causing distress to spatially extended infrastructures, such as the Pavoncelli hydraulic tunnel (Cotecchia et al. 1990), the major hydraulic infrastructure that supplies water toward the Apulia region.

As a consequence of the limited number of analog strong motion records and of the lack of extensive ground deformation measurements, many questions are still open on the potential impact of a repetition of a similar earthquake from one of the many active normal-type faults of this region. Indeed, the impact may be relevant up to the urban area of Napoli, which, although lying at some tens of km away from the seismogenic source, experienced in 1980 the collapse of several buildings with a large number of fatalities.

In this study, starting from the relatively limited information available, a regional-scale 3D PBS of the earthquake ground motion within the broader Irpinia area was carried out. The simulation domain covers a wide area, encompassing different regions (mainly Campania and Basilicata), which suffered significant shaking intensity and physical damage in the 1980 earthquake. This is shown in Figure 1, where the macroseismic intensities according to the Mercalli–Cancani–Sieberg scale (I_{MCS}, from Locati et al. 2022) are illustrated, together with the causative seismogenic faults of the earthquake, as well as other active faults mapped in the Database of Individual Seismogenic Sources (DISS 2025). The epicenters of the historical earthquakes in the region with $M_W \geq 6.0$ (from Rovida et al. 2022) are also pointed out. The PBS were performed using the spectral element code SPEED (Mazzieri et al. 2013), which has been extensively used in the recent past to simulate earthquake ground motions from various real or scenario (hypothetical) earthquakes in different regions worldwide, in most cases validated by station-by-station comparisons with the available seismic records (e.g., Paolucci et al. 2015; Evangelista et al. 2017; Infantino et al. 2020; Smerzini et al. 2023). From such PBS, a validated dataset of near-source simulated ground motions was constructed, named the BB-SPEED set (Paolucci et al. 2021; Smerzini et al. 2024), aiming at providing a complement to records for seismic analyses of structures or geotechnical systems.

After illustrating the setting and the main features of the numerical model, the simulated ground motions are compared with the available analog recordings both in the time and frequency domains, as well as with the observed macroseismic field. Subsequently, the near-source features of ground motion are investigated, including attenuation with distance,

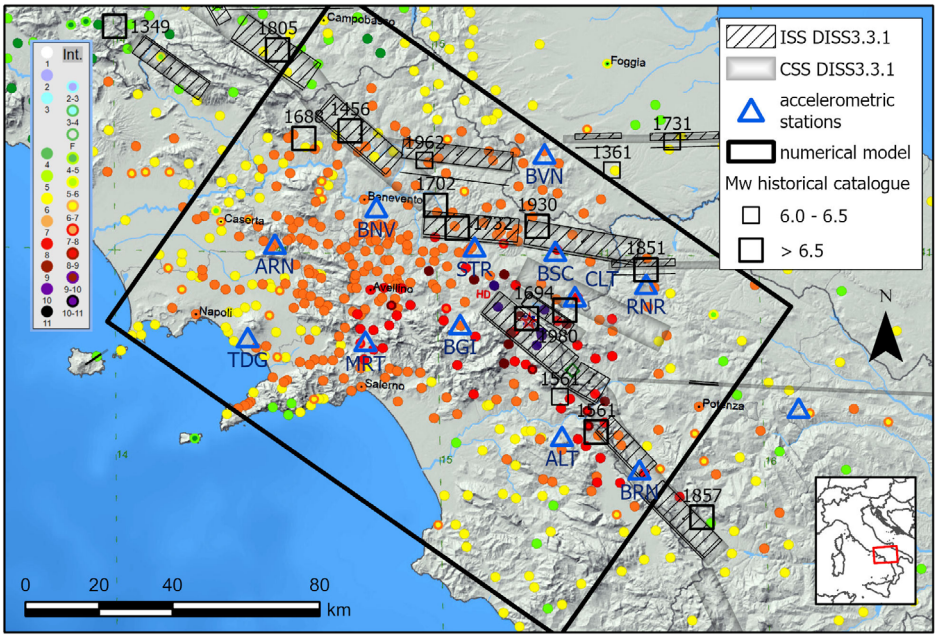

FIGURE 1 | Map including the region hit by the Nov 23, 1980, Irpinia earthquake, with the Macroseismic Intensities (I_{MCS} from Locati et al. 2022). The black rectangle delimits the extent of the numerical model developed in this study. The gray rectangles show the Individual and Composite Seismic Sources (ISS and CSS) according to the Database of Individual Seismogenic Sources DISS (2025). Blue triangles are the accelerometric stations that recorded the 1980 earthquake (records available from the ITACA database https://itaca.mi.ingv.it/). Historical earthquakes with $M_W \geq 6.0$, from Rovida et al. (2022), are shown by black squares.

spatial distribution of permanent ground deformation, features of impulsive signals, fault-related polarization, and up-dip directivity effects.

2 | Set-up of the Regional-Scale 3D Numerical Model

2.1 | The Seismic Velocity Model

3D PBS relies on the available geological and geophysical characterization of shallow crustal layers, constraining the definition of a wave propagation velocity model (in terms of S and P wave velocities, V_S and V_P) as well as an anelastic attenuation model (in terms of Q factors). Extensive hydrocarbon explorations in the Southern Apennines since the 1980s (Ascione et al. 2020; Porfido et al. 2022) have provided seismic reflection and well data, which have supported the definition of structural models of the Southern Apennines and the reconstruction of its tectonic evolution. The subsoil model used in this study (shown in Table 1) considers only the rock crustal layering, up to an outcropping engineering bedrock characterized by a $V_{s,30}$ of about 800 m/s, following the model proposed by Ameri et al. (2011) and then slightly modified by Cauzzi et al. (2012). The shallower layers of this crustal model represent the sedimentary sequence of the Bradano Through Quaternary deposits, while the deepest ones belong to the Apulia Carbonate Platform (Improta et al. 2003).

TABLE 1 | Crustal model adopted in the numerical simulations. $V_P = 1.81 \cdot V_S$ is assumed for all layers. A frequency-dependent attenuation model ($Q = Q_o * f / f_o$), with a reference frequency f_o = 1 Hz and Q_0 values for S waves as given in the table, is adopted.

Thickness, m	ρ, kg/m^3	V_S, m/s	Q_0 ($f_0 = 1$ Hz), -
1000 (*)	$1960 + 11\ z^{0.5}$ (**)	$700 + 39\ z^{0.5}$ (**)	70
1000	2300	1930	70
2000	2500	2490	210
6000	2600	3150	420
12 000	2700	3590	420

(*) variable thickness (≥1000 m) depending on ground surface elevation. (**) depth z is calculated from ground surface.

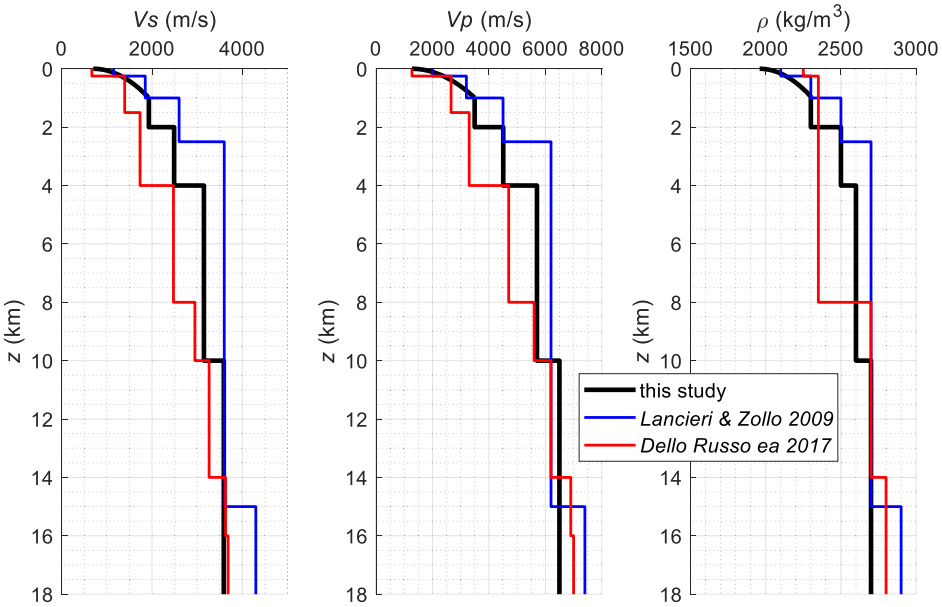

FIGURE 2 | S-wave velocity V_S, P-wave velocity V_P, and mass density ρ profiles adopted in this study (black thick lines). The blue and red lines show profiles from literature studies (Lancieri and Zollo 2009 and Dello Russo et al. 2017, respectively).

As specified in Table 1, parabolic profiles were introduced for V_S, V_P, and mass density ρ as a function of depth z from the ground surface, to characterize the smooth increase in the soil properties in the first 1 km. Note that the 1D velocity model of Table 1 was used throughout the computational domain, with the depth of the different soil layers changing locally according to the topography, the latter one having been shaped according to a Digital Elevation Model (DEM) with 30 m resolution. For all geologic layers, the values of V_P were calculated as $1.81 \cdot Vs$, corresponding to a Poisson's ratio $\nu = 0.28$. Figure 2 shows the modeled V_S, V_P, and ρ profiles in comparison with other literature studies (Lancieri and Zollo 2009; Dello Russo et al. 2017).

After a sensitivity analysis to fit the ground motion attenuation features observed during the 1980 earthquake, a frequency-proportional quality factor Q was considered ($Q = Q_o \cdot f/f_o$), with the reference frequency $f_o = 1$ Hz and the corresponding Q_o values for S waves as shown in Table 1. Details for the numerical implementation of the frequency proportional Q model are provided in Stupazzini et al. (2009). Such frequency dependence of Q was also assumed by Rovelli (1983), who estimated for the shallow crustal layers $Q = 40f$, in one of the first attempts at calibration of Q values from the Irpinia earthquake accelerometric records. With respect to Rovelli's estimates, slightly larger values of Q were adopted in the PBS to capture some relevant patterns of distant ground motion records, such as Torre del Greco (TDG, see Figure 1). For the same reasons, the frequency-dependent Q model was preferred to the frequency-independent Q model, that was suggested by other authors (e.g. Zollo et al. 2014) for the path attenuation effect in the same area.

2.2 | Mesh and Computational Features

As shown in Figure 1, the numerical model covers an extended region of the Southern Apennines for a total of 147×110 km^2. This was done to explore the variability of ground motion within a relatively large area, including different locations, such as the towns of Napoli (NW of the model) and Potenza (SE), with the perspective of using this PBS for seismic risk assessments at an urban scale for a potential repetition of an earthquake similar to the 1980 event. The depth of the model, 22 km, was set to encompass a sufficiently large portion of the Earth's crust, allowing for future use of the model in the simulation of rupture processes associated with other seismic events. An overview of the computational domain, meshed with hexahedral spectral elements, is given in Figure 3.

Table 2 lists the computational features of the mesh. A spectral degree 4 has been used for all simulations, allowing for a frequency resolution of about 2 Hz, which was verified by a dedicated series of sensitivity analyses, as well as by verifications using the Hisada and Bielak (2003) approach, not documented herein for the sake of brevity. Simulations were performed on the CINECA, Italy, High Performance Computing (HPC) platform Galileo

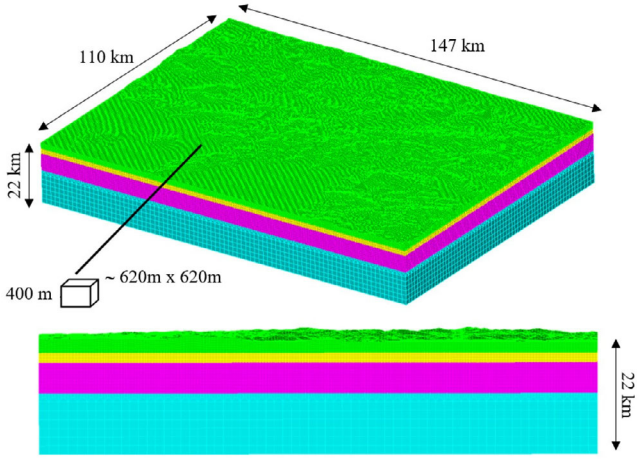

FIGURE 3 | 3D view (top) and 2D lateral view (bottom) of the computational mesh adopted, with a detail of a 3D spectral element at the ground surface.

TABLE 2 | Computational features of the simulations done with SPEED code.

Model size	Frequency resolution	Number of spectral nodes, $SD = 4$	Computational time step	Simulation duration	Computational time
110 km × 147 km × 22 km	2 Hz	~67 M	0.001 s	80 s	4.14 hours

Note: SD is the polynomial Spectral Degree adopted. The computational time refers to the use of 384 cores on the HPC G100 system of computer centre CINECA, Italy (https://www.cineca.it/).

(https://www.hpc.cineca.it/systems/hardware/galileo100/), using 384 cores. This allowed us to complete 80 s of the simulation of the 1980 earthquake in about 4 hours.

2.3 | Kinematic Features of Seismic Source Models

To constrain the source model, we relied on the information coming from literature (e.g., among others, Bernard and Zollo 1989; Westaway 1993; Ameri et al. 2011; Dello Russo et al. 2017), according to which the 1980 earthquake involved the rupture of 3 fault segments, with a time-lag of about 20 s each. For ease of calculation, Ameri et al. (2011) limited their study to the single-segment source rupturing at 0 s. Figure 4 shows the geometry of the fault planes used for the simulations, with geometric parameters reported in Table 3. The distribution of the total magnitude (M_W 6.8, as reported in the most recent version of the CPTI15 catalog, Rovida et al. 2022) among the different fault planes was based on Bernard and Zollo (1989).

The kinematic source model requires defining the spatial and temporal evolution of the co-seismic slip on the fault plane and the location of the nucleation point. This is achieved by introducing, for each sub-fault in which the fault plane is discretized, a suitable slip time function (STF), parametrized in terms of the rise time (τ), the rupture time (T_R), or, alternatively, the rupture velocity V_R.

The STF adopted in this study for each subfault has the exponential form shown in Equation (1), where $f(t)$ is the slip velocity, τ is the rise time (that is, the time required for the slip to reach 90% of its final value), and T_R is the rupture time:

$$f(t) = \frac{(t - T_R)}{(\tau/4)^2} \exp\left(-4(t - T_R)/\tau\right) \quad (1)$$

Note that the geometry of the fault plane is not directly designed inside the numerical domain, as the code SPEED allows for the use of a "not-honoring" strategy for the assignment of the kinematic parameters (amplitude, rupture, and rise time of the seismic moment time function) of the discretized sub-faults to an arbitrary set of nodes. This approach makes the

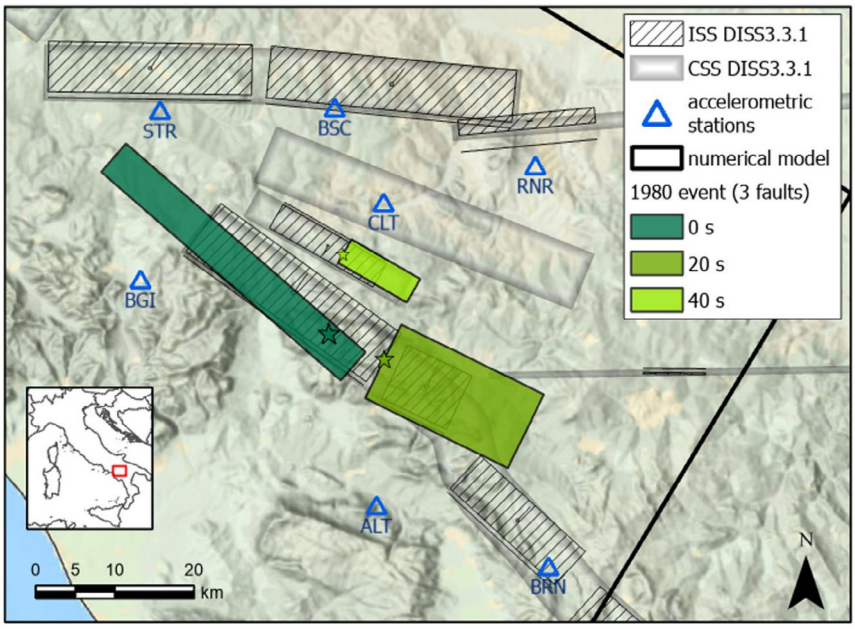

FIGURE 4 | Map of the fault segments (in green) used to simulate the multi-rupture 1980 earthquake, including the nucleation points for each segment, the accelerometric stations, as well as the individual and composite sources of the DISS database (DISS 2025).

TABLE 3 | Geometric and kinematic properties of the 3-fault source model adopted in the simulation.

M_w	M_o, Nm	Segment	Strike, °	Dip, °	Rake, °	L × W, km²	Top depth, km	Nucleation point: lat, lon, °; depth, km
6.8	$8.7{\cdot}10^{18}$	0 s	315	60	270	40 × 9.5	2	40.75, 15.34; 8
	$4{\cdot}10^{18}$	20 s	300	20	270	20 × 11	8	40.72, 15.42; 10
	$3{\cdot}10^{18}$	40 s	124	70	270	10 × 10	2	40.84, 15.37; 8

code flexible to deal with multiple fault rupture realizations, as the same computational mesh can be used with different sets of loaded spectral nodes, that is, different sets of assumed fault ruptures.

Figure 5 shows details of the slip distribution models adopted on each fault segment, borrowed from Ameri et al. (2011), based on the source inversion study by Cocco and Pacor (1993), for the main segment, and from Dello Russo et al. (2017)

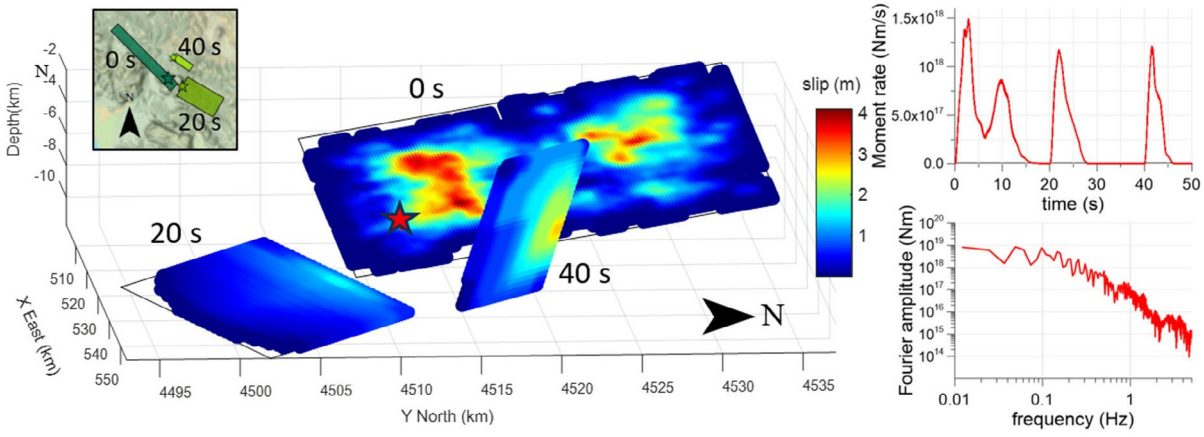

FIGURE 5 | Left: 3D view of the slip distributions adopted on the 3 fault segments used for the simulation of the 1980 earthquake. The hypocenter on the main fault is shown by a red star. Slip distributions are from Ameri et al. 2011 (for the main segment) and Dello Russo et al. 2017 (for the smaller segments, with 20 s and 40 s rupturing delay). The kinematic features of the different fault segments are given in Table 3. Right: total moment rate function of the source in time and frequency domain.

for the smaller segments. According to the former study, the slip on the main fault is characterized by two main asperities, the largest one located close to the Southern edge of the fault and the other one located close to the Northern edge, both at a depth between 6.5 and 11 km. Note that the dip of the 40s fault plane is antithetic to the 0s and 20s fault planes (Westaway 1993). The rupture velocity adopted for the simulations is $V_R = 0.8Vs$. For the exponential STF, a constant rise time $\tau = 0.5$ s was assumed, consistent with the frequency resolution of the mesh.

2.4 | High Frequency Enrichment

To generate broadband (BB) ground motions beyond the simulation frequency resolution threshold of 2 Hz, the results were post-processed using the ANN2BB approach, introduced by Paolucci et al. (2018b) and later revisited in Paolucci et al. (2021). Leaving a detailed introduction of the method to the above references, it is sufficient here to recall that the approach consists of training an artificial neural network (ANN) based on strong ground motion records, suitable to estimate, from the SPEED long-period response spectral ordinates, the corresponding short-period values and, thus, to construct a BB response spectrum. BB time histories are then obtained by merging SPEED waveforms at low frequency with a stochastic signal at high frequency, the latter being suitably scaled so that its response spectrum approaches the target one given by the ANN. A merging period $T^* = 0.5$ s was selected to glue the short and long period ranges, consistent with the maximum frequency resolution. Finally, it is worth noting that such ANN2BB procedure does not alter the long-period content of the SPEED simulations beyond T^*, so that the remarks on the near source features presented in the following sections are not affected by such processing, since they are governed by the long-period ground motion.

3 | Simulation Results and Comparison With Observations

3.1 | Introduction

One of the main advantages of PBS, with respect to empirical GMM, is the availability, in addition to peak values of motion, of a comprehensive picture of the spatial and temporal evolution of earthquake ground motion. An example of results is provided in Figure 6, where snapshots of the simulated velocity wavefield (EW component) are portrayed for different instants of time, showing the progress of the seismic wavefield with the different phases of the multi-segment rupture. Namely, because of the selected location of the cross-section BB' considered in Figure 6, it is possible to clearly distinguish the late rupture of the 40 s segment, which occurred right along the cross-section. The 20 s event is not evident from this cross-section, because of the Southward directivity of the second event. Such complexity is also underlined by Figure 7, showing the time series of displacement (fault parallel, FP, and vertical, UD, components), along a cross-section throughout the area subjected to the various rupture episodes.

For the comparison of the simulation results with the available observations of the 1980 earthquake, the set of analog accelerometric stations that were in operation at the time of the earthquake, shown in Figure 1, was considered. Records are available from the Engineering Strong-Motion Database (ESM, https://esm-db.eu/, Luzi et al. 2020) of the Italian

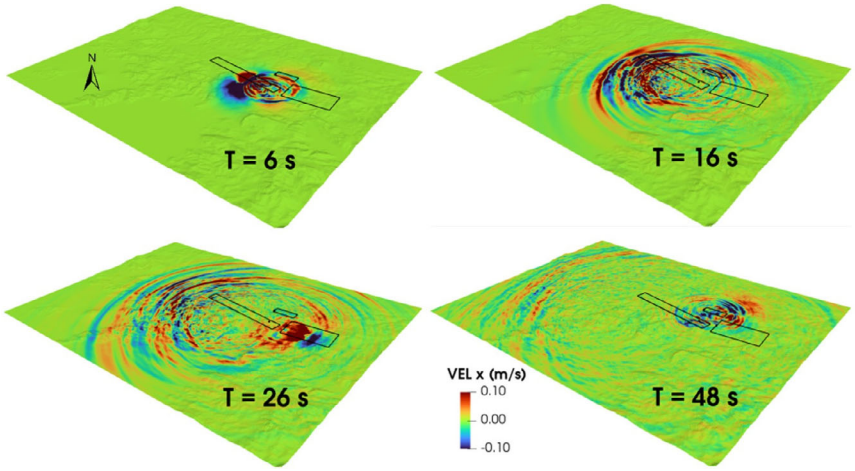

FIGURE 6 | Snapshots of EW simulated velocity wavefield showing the activation of the three fault segments (starting at 0, 20, and 40 s, respectively).

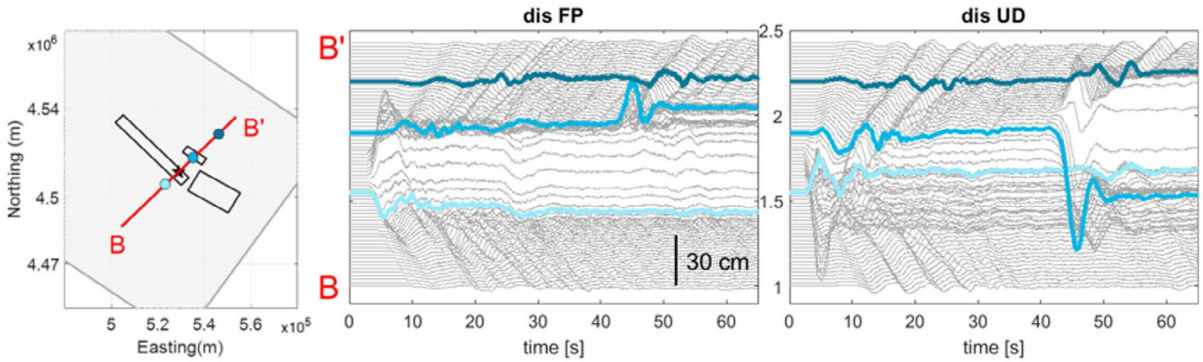

FIGURE 7 | Simulated displacement time histories along the BB' cross-section shown in the box on the left, for fault-parallel (FP) and vertical (UD) components. Results at three near-field locations are highlighted in shades of blue.

Institute of Geophysics and Volcanology (INGV). In such comparison, it should be recalled that, as for any PBS of an historical earthquake, the input information will generally lack details of both the soil and crustal properties over a large spatial extent, including viscous and scattering attenuation, as well as of the kinematic source model, where the position of local rupture asperities may strongly affect the ground motion, especially at near-source stations. Although, for these reasons, the comparison with records cannot be regarded as a validation in strict sense, a quantitative evaluation of the misfit between simulated and recorded motions is proposed in the following, in addition to more qualitative checks regarding the visual inspection of results, in both time and frequency domain, as well as the spatial distribution of the simulated ground shaking field with respect to the observed macroseismic intensities.

3.2 | Comparison With Recorded Time Histories and Response Spectra

Figures 8 and 9 show the comparison between the simulated (BB) and recorded velocity time histories, as well as the corresponding Fourier and acceleration response spectra, at selected stations, namely, Calitri (CLT), Sturno (STR), Bisaccia (BSC) and Torre del Greco (TDG), located at a distance R_{epi} of 19 km, 33 km, 28 km and 78 km, respectively, from the epicenter of the initial rupture. The location of these stations is shown in Figure 1. A reasonable agreement between recorded and simulated motions is found, on the horizontal as well as on the vertical component, showing the effect of the successive fault rupturing (note in particular station CLT, lying close to the third fault). Note that the analog records are band-passed filtered in a f_l-f_h range, where f_l and f_h typically lie in the interval 0.1–0.2 Hz and 25–30 Hz, respectively. Simulated motions in these plots are not filtered.

To assess quantitatively the agreement of the simulations with respect to records, in terms of response spectral ordinates, Figure 10 (*top*) shows the logarithmic residuals, computed as $\log_{10}$(Sim/Rec), for the horizontal components, extended to all available recording stations. A good agreement is found for all considered periods, with the single exception of $T = 2$ s, for which there is a tendency of overestimation of simulations with respect to records, which is discussed later. It is also worth to mention the excellent agreement in terms of the average spectral ordinate SA_{avg}, computed in the 0.2–1 s period range, that was found in several studies as an efficient and sufficient ground motion intensity measure for fragility studies (e.g., Kohrangi et al. 2017). This outcome confirms the effective potential use of the results of these simulations for applications of regional-scale seismic risk assessment in the study area.

The similar residual computation for the UD component (Figure 10, *bottom*) shows a slight systematic overestimation of simulation results with respect to records. Although from the engineering and risk assessment applications, this bias has no practical relevance, it demonstrates that some modeling assumptions regarding the UD component should be revisited, more likely in terms of the P-wave Q factor, which was assumed to be twice that of S-waves.

3.3 | Peak Ground Shaking Maps

Figure 11 shows ground shaking maps of simulated peak ground acceleration (PGA) and velocity (PGV) for the geometric mean of the horizontal components, together with the recorded peak values at the available accelerometric stations, the latter ones denoted by a dot with the corresponding color scale. As a further term of comparison, the isoseismal maps of the Irpinia earthquake, expressed in I_{MCS} degrees, are also plotted, based on the compilation by Postpischl et al. (1985). Despite the large spatial scale encompassed by the numerical simulations, the uncertainties

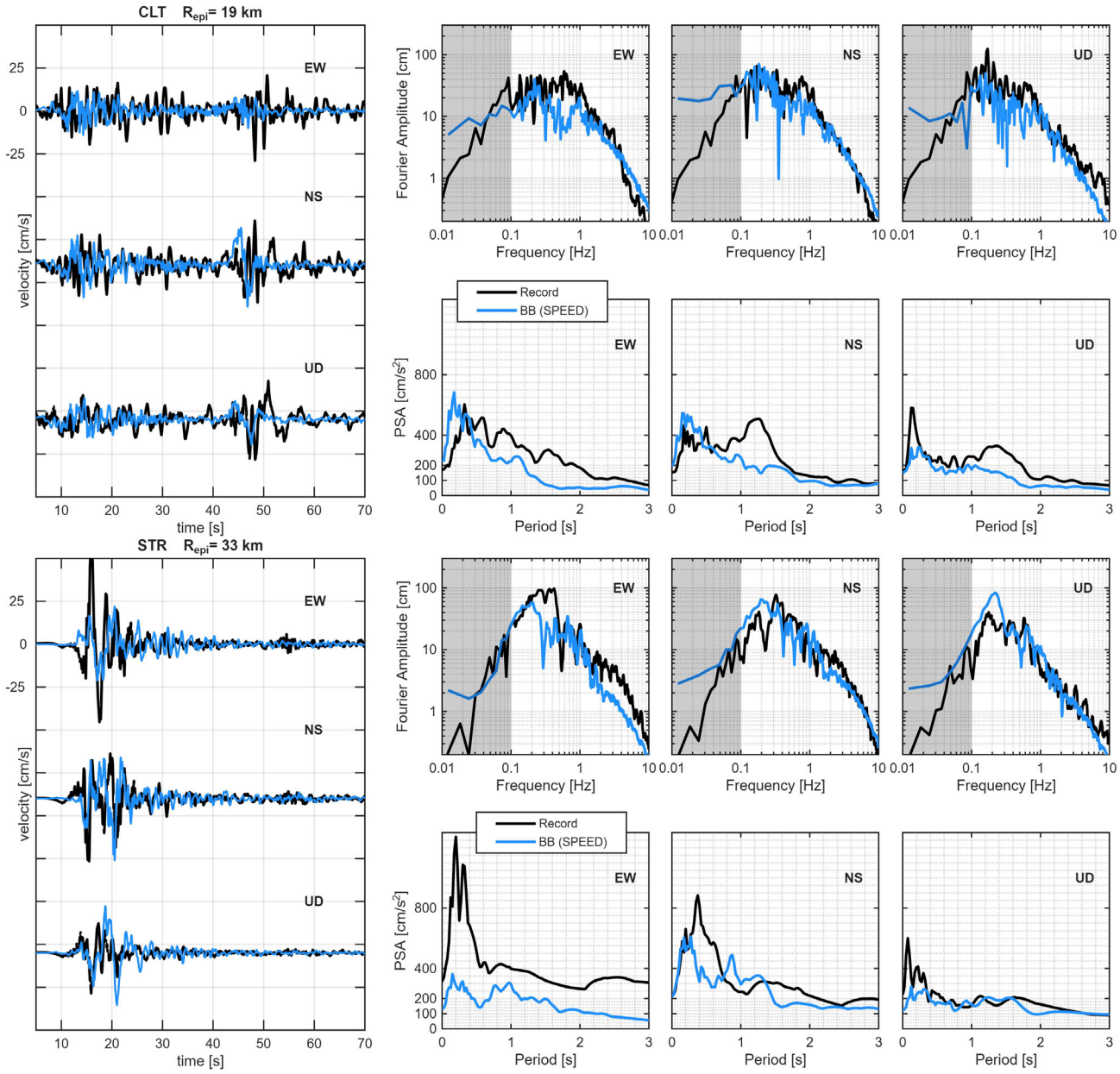

FIGURE 8 | Simulated broadband (blue) and recorded (black) ground motion in time and spectral domain for CLT and STR, stations at respectively, 19 and 33 km from the epicenter. Velocity time histories are shown with respective Fourier and acceleration response spectra. No filtering has been applied to simulations. The shaded area highlights frequency ranges where records have been filtered.

in the definition of the kinematic fault model, and the relatively rough modeling of the site conditions, it can be noticed that a realistic spatial distribution of ground motion is obtained, in reasonable agreement with both recorded values and with the observed damage levels. As a reference, according to the correlation of Italian macroseismic data with recorded peak values of ground motion made by Gomez-Capera et al. (2020), the VIII degree of the MCS scale corresponds to an average PGA value of about 2 m/s^2 and to an average PGV of about 0.12 m/s, that is reasonably close to what is obtained from simulations, with a similar pattern of attenuation with respect to the main and secondary faults of the earthquake. This supports the conclusion that, although a detailed agreement with the recorded time histories is out of reach, because of the uncertainties mentioned previously, as well as of the sparse information for an earthquake occurred more than 40 years ago, a realistic picture of ground motion can be achieved through the PBS, with the potential of both a better understanding of near-source ground motions, as illustrated in the following sections, and of investigating the potential impact of the repetition of such an earthquake, or of other possible ones, that is the object of a study in progress.

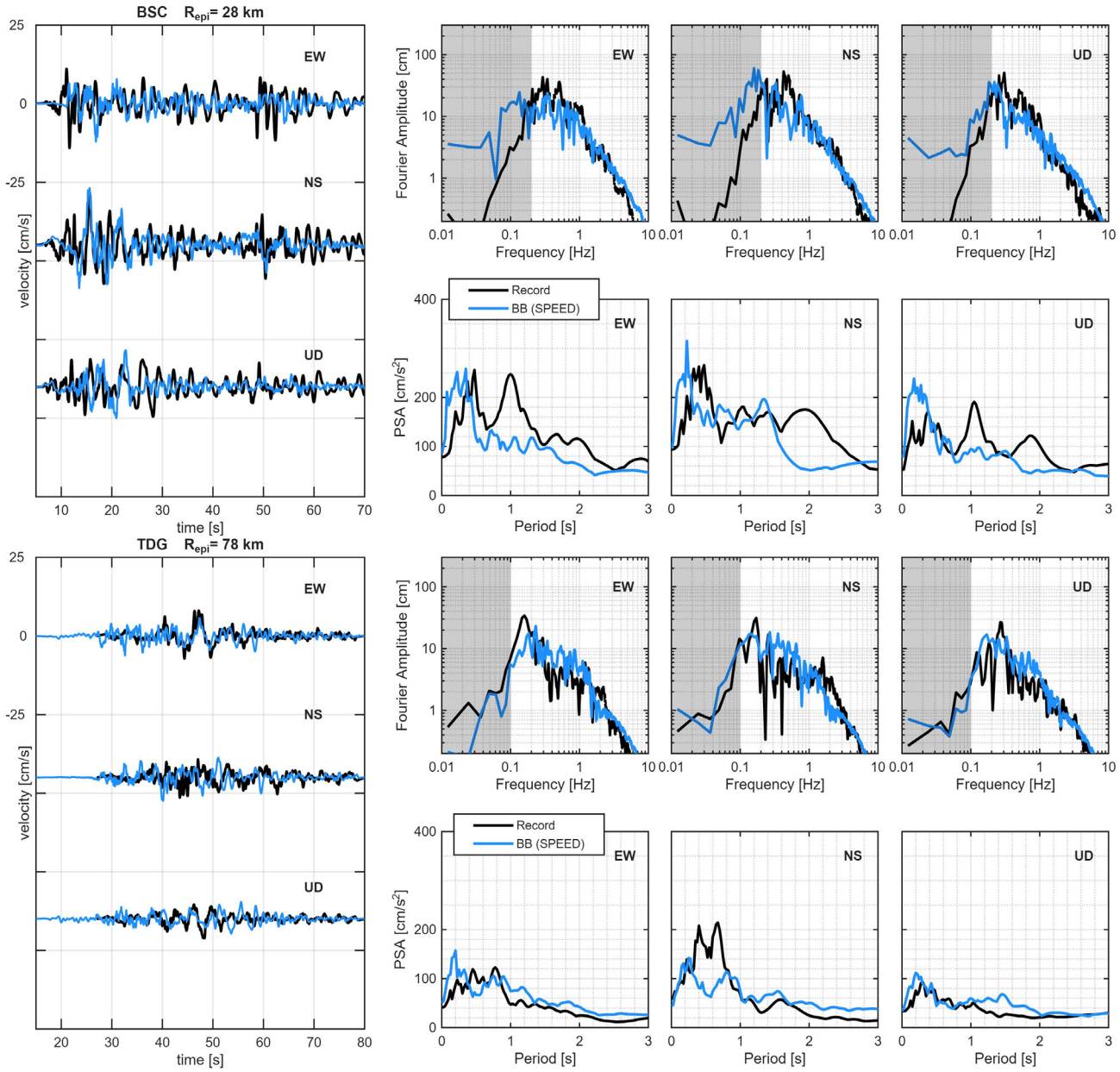

FIGURE 9 | Same as in Figure 8 for BSC and TDG stations, respectively, at 28 and 78 km from the epicenter.

3.4 | Permanent Ground Deformation

Among the variety of information on near-source ground motions that can be extracted by a PBS, the permanent ground displacement field is a notable one, with potential practical implications on the estimation of the relative displacements of adjacent points of extended structures and infrastructures (such as bridges, pipelines, rails) as well as on the corresponding straining levels.

Figure 12 shows the maps of permanent ground displacements (PDIS) for the horizontal (H) and vertical (UD) components. As a term of reference, the vertical throws measured at some locations on the 1980 fault scarp (Pantosti and Valensise 1993) are superimposed on the map, showing a reasonably good agreement with simulations. In the H case, the map plots the absolute value of displacement, with amplitude and direction denoted by arrows. Although no measurement was available at that time to verify the H motion, it is interesting to point out the patterns of the horizontal displacement, the direction of which is consistent with the focal mechanism far from the source, inducing an extensional ground motion on the footwall (to the South–West) and hanging wall (to the North–East) sides. Instead, above the fault surface projection, the permanent displacement field demonstrates its complexity, especially where the slip distribution has its main asperities (Figure 5). In the interpretation of these results, it should be recalled that these displacements are

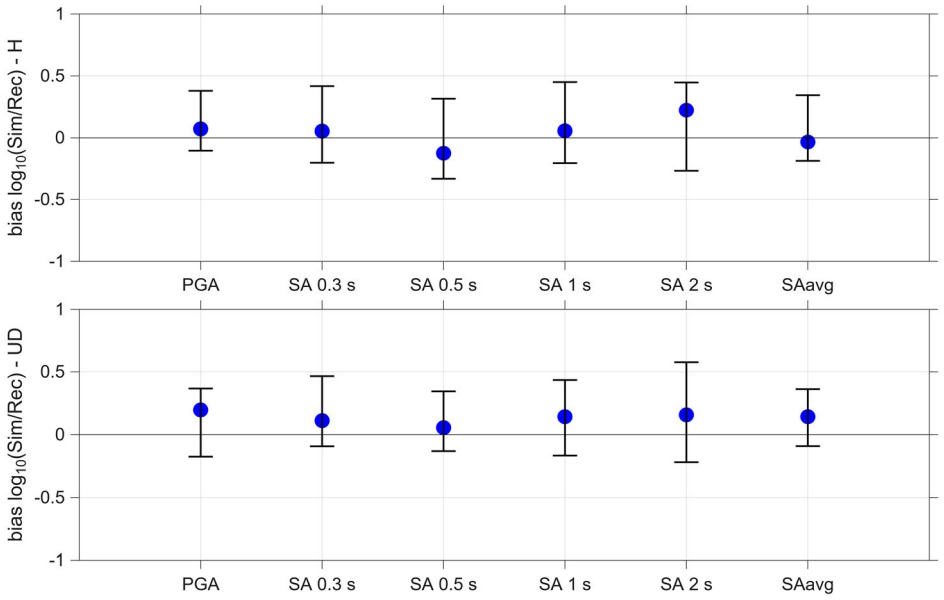

FIGURE 10 | Residuals of simulated vs recorded response spectral ordinates of the horizontal (H, top) component (in rotD50) and vertical (UD, bottom) component. On the right-hand side of the figure, the results are shown in terms of SA_{avg}, defined as in Kohrangi et al. (2017). Residuals are computed in log10 scale, considering all stations with available records of the 1980 earthquake.

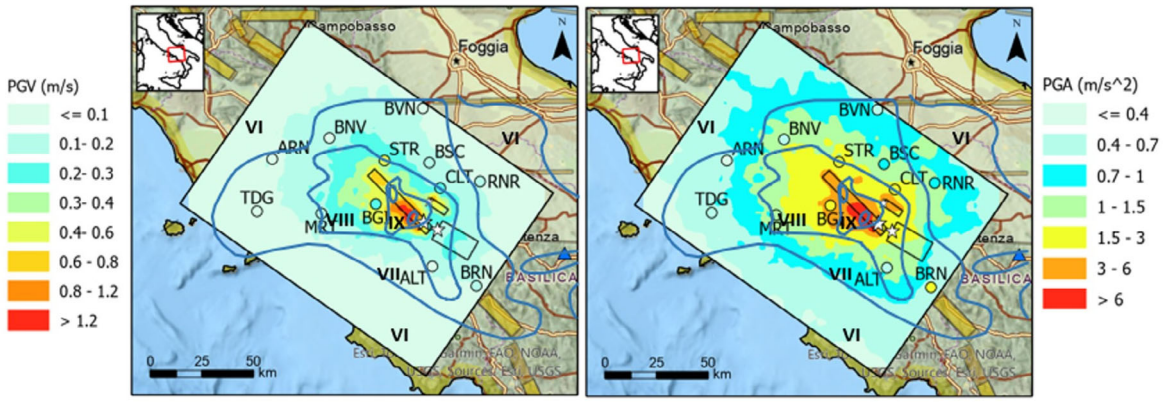

FIGURE 11 | Maps of simulated PGV (left) and PGA (right) for the horizontal (geometric mean) component of ground motion. The superimposed colored dots show the recorded peak values at the available accelerometric stations (with the same color palette as for the map). Isoseismal lines of the 1980 earthquake are also plotted, according to Postpischl et al. (1985).

related to an elastic dislocation with a continuous strain distribution, which can only approximate the finite surface ground offset observed in the earthquake.

3.5 | Attenuation of Ground Motion With Distance

In Figure 13, the simulated rotD50 values (i.e. median of rotated amplitudes) of PGV and PGA are compared both with the corresponding recorded values during the Irpinia earthquake and with other near-source worldwide records available in the NESS2.0 dataset from Sgobba et al. (2021a), within the M_W 6.7–6.9 range and stiff site category (A or B, according to the Eurocode 8, CEN 2004). On the same plot, the GMM by Lanzano et al. (2019) calibrated on records from Italian crustal earthquakes, and adjusted for a near-source correction factor (based on NESS dataset, Sgobba et al. 2021a), referred to as $ITA18_{NESS}$, is also shown (median and corresponding dispersion band $\pm\sigma$), for M_W 6.8 and $V_{s,30} = 800$ m/s. Note that this comparison is slightly biased by the presence of the three fault segments for the Irpinia earthquake: in this case, the distance metric, that is the Joyner–Boore distance (R_{JB}), is defined by the minimum distance of the site with respect to any of the surface projections of each segment. For a more quantitative comparison, Figure 14 shows the corresponding

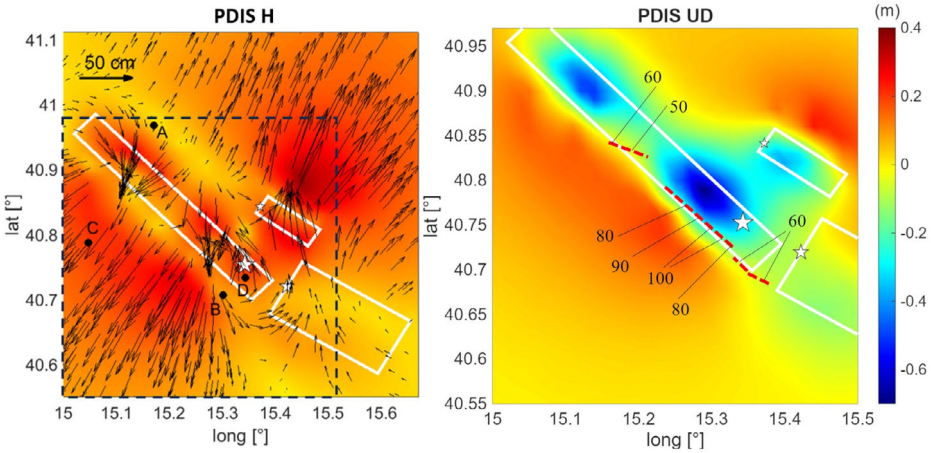

FIGURE 12 | Maps of the simulated permanent displacement (PDIS) for the horizontal component (H, left), with the arrows denoting the amplitude and direction of motion, and for the vertical component (UD, right). In the right panel, the trace of the 1980 fault scarp (red dashed line), with measured vertical throws in cm, modified from Pantosti and Valensise (1993), is superimposed on the PDIS plot. Note that the vertical plot refers to an area of reduced size with respect to the horizontal plot, as delimited on the left by the black, dashed, square. A, B, C, and D (in the left panel) show the location of sites discussed in Section 4.

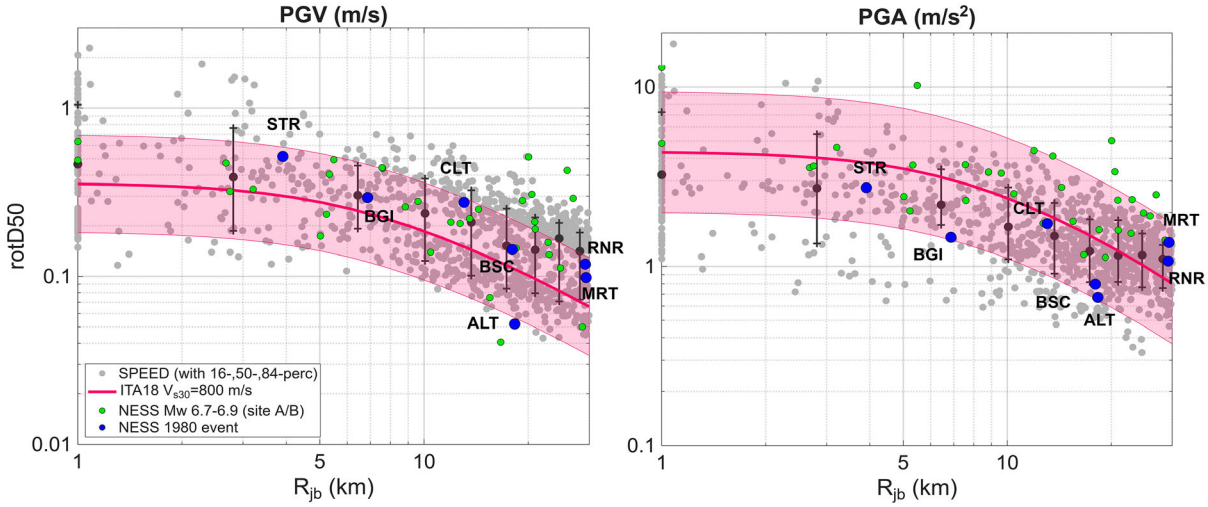

FIGURE 13 | Attenuation as a function of R_{JB} distance of simulated rotD50 PGV and PGA (gray dots), compared with recorded values of both the Irpinia 1980 earthquake (blue dots) and of other worldwide events of similar magnitude ($6.7 \leq M_w \leq 6.9$) (green dots), as given from the NESS2.0 database (Sgobba et al. 2021a), for comparable ground type (categories A or B of Eurocode 8). The corresponding empirical predictions (median ± 1σ) from the $ITA18_{NESS}$ ground motion model (Sgobba et al. 2021a) are also shown (M_w 6.8, $V_{s,30} = 800$ m/s).

residuals as a function of period, computed as logarithmic differences (δ_{log10}) of the recorded versus simulated values with respect to the reference $ITA18_{NESS}$ model, and for three intervals of distance, i.e., $R_{JB} \leq 1$ km representing points above the surface fault projections, 1 km $< R_{JB} \leq 10$ km representing intermediate near-source distances, and 10 km $< R_{JB} \leq 30$ km up to the limit of the near-source area of the Irpinia earthquake. Positive residuals correspond to recorded/simulated values larger than the $ITA18_{NESS}$ model. The average of simulated residuals is denoted by a black line, blue dots correspond to the residuals of Irpinia records, while green dots correspond to the other records of NESS2.0 in the same magnitude and distance range, as well as site categories. These results show that there is a tendency of our PBS to overestimate the median empirical GMM at intermediate to long periods, within a distance range $R_{JB} < 30$ km, although this tendency is also present in a significant fraction of the available records of the Irpinia earthquake. This overestimation is probably because of an excess of coherence of the kinematic source model, which considers constant values of rupture velocity and rise time. The relatively large simulated values of PGV close to the main asperity (1–2 m/s) are likely related to the assumption of constant rise time. Adopting a direct correlation of rise time and slip, such as in the Graves and Pitarka (2016) rupture generator, instead, would lead to longer rise times at the asperities and consequently lower

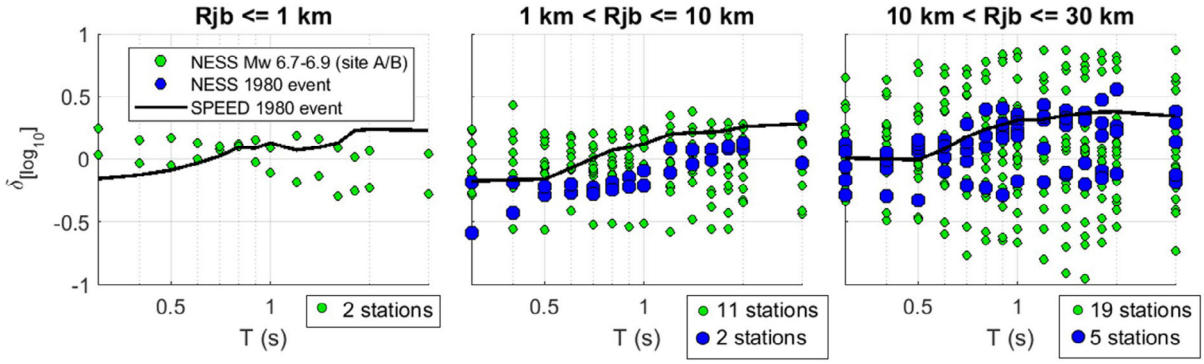

FIGURE 14 | Residuals with respect to $ITA18_{NESS}$, as a function of period and distance ranges. The average residual for simulated ground motion is shown by a black line, the residuals of the NESS2.0 Irpinia 1980 stations by blue dots, while those of the NESS2.0 stations (with comparable magnitude and site conditions) by green dots.

amplitudes of ground motion. Finally, we note that, in the short-period range, spectral values are in good agreement both with the $ITA18_{NESS}$ and with the available Irpinia records.

4 | Near-Source Effects: Ground Motion Impulsive Features and Polarization

Ground motions recorded in the near-source region may have peculiar features in terms of amplitude, duration, frequency content, and polarization owing to the strong influence of the characteristics of the fault rupture process. These include the fault geometry relative to the site, focal mechanism, slip asperity, hypocenter location, and rupture velocity. Sites in the near-fault region may exhibit pulse-like motions in which much of the seismic energy is concentrated in a velocity cycle with predominant period T_P (Somerville et al. 1997). Double-sided pulses in the velocity time series are often observed in the forward directivity region, i.e., where the rupture front propagates toward the site, and are most pronounced on the fault normal (FN) component for strike-slip faults (Somerville et al. 1997; Baltzopoulos et al. 2020; Yen et al. 2021). Other physical phenomena can influence the impulsive characteristics of ground motion, as those associated with the fault static offset (Somerville et al. 1997; Dreger et al. 2011; Kamai et al. 2014), i.e. the so-called fling step, which corresponds to a one-sided pulse in the velocity time series (Bolt 2010). It is recognized that impulsive ground motions have a damage potential substantially different from that of ordinary motions due to the peculiar amplification of both elastic and inelastic structural response over a narrow band of periods around T_P (Somerville et al. 2003; Iervolino et al. 2012; Baltzopoulos et al. 2015; Sgobba et al. 2021b).

Whereas the pulse-like features of ground motions originated by very large strike-slip events have been studied extensively, less efforts have been made to investigate the behavior of near-source ground motions from dip-slip normal faults. Providing a complete description of the seismic wavefield in the near-source region, this PBS study may add some interesting insights into such features. For this purpose, the pulse-like waveforms were identified, and the corresponding T_P values were computed by applying the wavelet-based algorithm of Shahi and Baker (2014). Figure 15 shows the maps of T_P (left) and of the corresponding θ (right), the latter ones corresponding to the orientation (azimuth) where the pulse is the strongest. Superimposed on the T_P map are the contour lines of *PGV*, computed along θ, while on the θ map, the FN/FP ratio of PGV is also illustrated.

According to these results, the following remarks can be made:

- impulsive motions are found predominantly in a region extending from the top edge of the fault, with an anisotropic pattern reflecting the rupture process (slip asperity relative to hypocenter location) and with very variable features in terms of maximum amplitude, orientation, and T_P;
- short period pulses (typically in the range 0.5 – 1.5 s) in the FN direction are predominant along the top edge of the fault, more specifically along the SE side (e.g., B and D sites), where they are associated with the largest PGV values, sometimes exceeding 1.5 m/s, as a consequence of up-dip directivity effects. Note that up-dip directivity was commonly found to dominate the strongest ground motions recorded during the recent normal fault Italian earthquakes (e.g., Tinti et al. 2014);
- long period pulses, typically in the range 4–6 s, are found predominantly North of the fault along the FP component (see cyan region on the right map) with lower PGV, of about 50 cm/s or less;

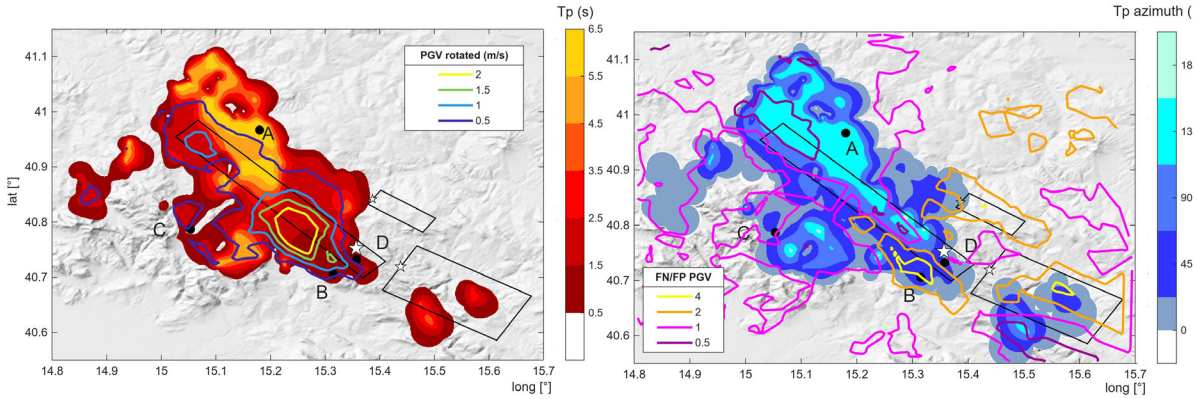

FIGURE 15 | Map of pulse periods, T_P (left panel), and of respective pulse azimuth θ (right panel). Black dots show locations A, B, C, and D of time histories receivers discussed in Figure 16. In the left panel, contours of PGV of horizontal simulated ground motion, rotated along the θ directions, are shown. In the right panel, the fault normal over fault parallel (FN/FP) ratios of PGV are superimposed on the map.

- the up-dip directivity region with the short period pulses is characterized by the largest FN/FP values of PGV (up to 4.5), while the FP component is prevailing, with FN/FP decreasing down to about 0.5, where the long period pulses occur;
- comparing the overall trends of T_P and PGV, and their spatial variability, it is clear that the damage potential of the near-source ground motion is sharply different, and it cannot be identified solely by its impulsive nature. Indeed, both T_P and PGV turn out to be highly variable, even at similar distances from the fault.

To provide further insights on the previous results, velocity and displacement time histories at a selection of receiver points are shown in Figure 16, together with the corresponding acceleration and displacement response spectra: B and C on the footwall (FW) side, A and D on the hanging wall (HW) side. B and D lie in proximity to the highest asperity region, close to the surface projection of the top edge of the fault. Although all selected receivers are identified as impulsive ground motions, at least in one direction, their features, in the time histories as well as response spectra, may be quite different. B and D are similar in their FN component, while the components with a prominent fling step are C (FN) and D (FP). At station A, the impulsive motion is identified in the FP direction, with a velocity pulse at about $T_P = 5$ s, the effect of which is also clearly visible in the peak of the displacement response spectrum (see the red arrow in Figure 16). We further note that, at B and D sites, the FN motion exhibits an intense amplification of response spectral demands at vibration periods between 0.5 and 1 s (as denoted by the arrows in the figure) that will correspond to larger inelastic spectral demands (e.g., Iervolino et al. 2012). At these two sites, which are located almost above and in the direction normal to the main asperity, a larger FN component is expected from the S-wave radiation pattern of the main asperity. Displacement response spectra show features that are well identified by the analytical spectral shapes derived by Faccioli et al. (2004) for impulsive and fling step motions. In the latter case, i.e., when the fling is dominant with respect to other vibratory effects (see D station, FP component), the displacement response spectral shape is monotonically increasing.

Other interesting features of the impulsive motions in the near-source region are found in Figure 17, which shows, on the left, the trend of T_P as a function of M_W, as obtained from the simulated scenario (colored blue dots), in comparison with the one from the NESS database of near-source recordings (black dots). The empirical relationship (green line and corresponding dispersion bands) by Shahi and Baker (2014) is also shown. Simulated T_P values range between about 1 s and 7 s for M_W 6.8, in substantial agreement with empirical evidence.

As also found from records, a large variability of T_P is found for an individual earthquake with a given M_W, as also pointed out by Yen et al. (2021). The amplitude and T_P of impulsive ground motions depend on the rupture characteristics such as slip and rupture velocity distributions, but also on the relative location of the receiver with respect to the fault (e.g., Akinci et al. 2024; Mavroeidis and Papageorgiou 2010). Considering, for example, the sites close to the main asperity on the east, such as sites B and D in Figure 15, where the seismic energy radiated from the asperity arrives in a short time window, the shortest T_P are obtained (between 0.5 and 1.5 s, see Figure 16). Clearly, using a different value of rise time would slightly change T_P (mostly in this region), but the overall patterns previously described would remain unchanged.

The trends of T_P as a function of PGD over PGV (in rotD50) are illustrated in Figure 17 (right panel) for the PBS of the 1980 event (colored blue dots) and for the NESS records (black dots). As commented previously, a very satisfactory

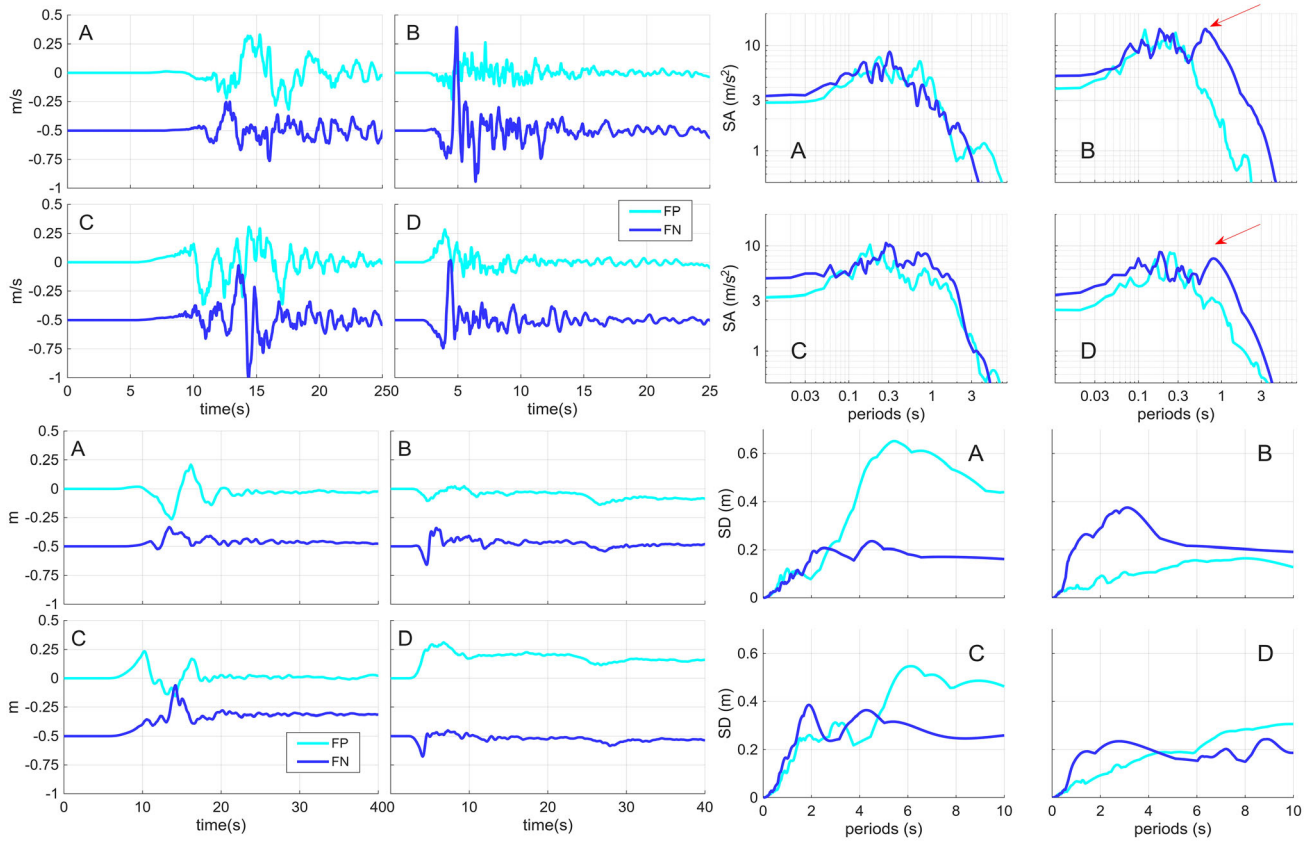

FIGURE 16 | Left panels: FP and FN simulated velocity (top) and displacement (bottom) time histories, at the reference locations shown in Figure 15. Right panels: response spectra of acceleration (top) and displacement (bottom) for the same reference locations. The red arrows point out the large amplification of the response spectra (between 0.5 s and 1 s) occurring at locations B and D.

agreement is found between our results and NESS within comparable M_W ranges. Superimposed on these plots, there also the closed-form analytical relationships reported by Paolucci et al. (2021) for T_P as a function of the ratio PGD/PGV, based on the analytical expressions of the "Ricker wavelet" (L1, cyan line), of the "double-impulse" (L2, dark blue line) and of

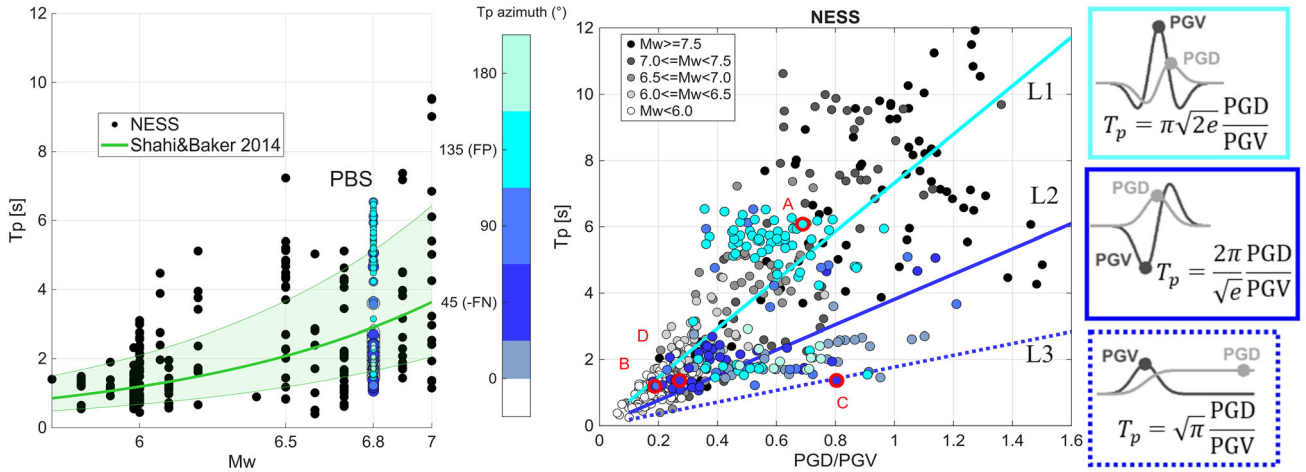

FIGURE 17 | Pulse period T_P calculated from the PBS of *Mw* 6.8 earthquake (colored using the blue color bar of pulse azimuth θ), compared with those computed from the NESS dataset, as a function of M_W (left panel) and of PGD/PGV (in rotD50, right panel). In the left plot, the empirical regression with respect to M_w from Shahi and Baker 2014 (Equation 21) is plotted in green. In the right plot, the positions of A, B, C, and D receivers of Figure 15 are highlighted in red. The linear relationships in the right panel plot were derived based on the analytical expressions of the "Ricker wavelet" (L1, cyan line), the "double-impulse" (L2, blue continuous line), and the "gaussian" (L3, blue, dotted line) functional forms.

the "gaussian" (L3, dashed line) functional forms. Note that the L2 waveform is the derivative of L3, and L1 is the derivative of L2. All the simulated as well as the observed points lie within the range identified by these three lines. This is also the case of the 4 stations pointed out previously: (1) A (FP component) and B (FN component) lie close to the L1 line, with a Ricker wavelet velocity pulse, made clearer by the double impulse in the displacement time history; (2) D (FN component) lies close to the L2 line (double impulse velocity and gaussian displacement); (3) C (FN component) lies close to the L3 line (gaussian velocity and fling step displacement). Note also that the largest fraction of long-period velocity pulses lies on the North side of the fault and are mostly FP directed.

Finally, it is worth to remark that there is no clear evidence of systematic differences at sites lying at either the HW or the FW sides of the fault, except for the obvious differences in terms of distance from the fault rupture. This is in agreement with the parametric study based on dynamic rupture simulations by O'Connell et al. (2007), who concluded that simple parameterizations based on the HW and/or FW position of the site may not be appropriate for normal faults with dips>50°, as the case considered in this paper for the Irpinia fault.

5 | Conclusions

In this research, we developed a large-scale 3D spectral element model, extending about 150 km in the longitudinal Southern Apennine chain and about 110 km in the transversal direction, surrounding the seismic faults that originated the devastating M_w 6.8 Nov 23 1980 Irpinia earthquake. Normal-fault earthquakes of $M_w \sim 7$ are considered as an upper bound along the Apennine mountain chain, but, owing to their relatively low frequency of occurrence (about 2–3 times per century in the past few hundred years of historical documentation of Italian earthquakes), a better understanding of the near-source ground motion associated with these events is a critical issue for an accurate quantification of seismic hazard.

The 3D numerical model was used to perform PBS of the Irpinia earthquake, accounting for a multi-segment kinematic source model rupturing in sequence three different faults, as identified based on past investigations, and on a relatively simple shallow crustal model including topography. At outcropping ground $V_{s,30}$ was set to 800 m/s, so that small-scale site amplification effects throughout the investigated area are not accounted for.

Quantitative comparisons with the available analog recordings showed a reasonably good agreement, in spite of the relatively limited information both on the seismic source model and on the ground properties, proving that the simulation results provide a realistic approximation of the temporal and spatial features of the ground motion occurred during the Irpinia earthquake.

These results allowed to shed light on some important features of near-source ground motions during a normal-fault earthquake including:

- the relevance of up-dip directivity effects, with significant polarization in the FN direction and short period pulses (T_P) in the interval of about 0.5–1.5 s, as pointed out in other recent normal-fault earthquakes in Italy (see, e.g. Chiocchiarelli and Iervolino 2010; Luzi et al. 2017);
- the dense presence of impulsive ground motions throughout the extension of the surface projection of the main fault, up to few km of R_{JB} distance;
- the sharp variability of T_P, ranging from about 0.5–1.5 s along the top edge of the fault and with the largest PGV values (FN component) above the main fault asperities, up to about 4–6 s, above the down-dip region, where FP motion prevails with lower amplitudes;
- the good agreement of the simulated T_P values as a function of PGD/PGV with the trend of recorded values available from the NESS near-source source dataset as well as from empirical relationships from literature (Shahi and Baker 2014);
- the good correspondence of the simulated displacement response spectral shapes with the analytical expressions for pulse-like motions (Faccioli et al. 2004);
- the possibility to obtain realistic evaluations of the three-component permanent displacement field, with potential applications to the seismic assessment of extended infrastructures, such as pipelines or high-speed railway lines.

Finally, this study supports the potential application of PBS of historical earthquakes as a tool for better calibrating fragility curves on observed damage, as demonstrated for the 2009 L'Aquila earthquake by Rosti et al. (2023)

and Monsalvo-Franco et al. (2025), as well as to provide realistic risk scenarios for future earthquakes, constrained on the specific tectonic and geological features of the study area (see, e.g., Stupazzini et al. 2021 for the Istanbul case).

Author Contributions

For this editorial all authors have contributed to the work reported. All authors have read and agreed to the published version of the manuscript.

Acknowledgments

The authors dedicate this paper to the memory of Antonio Rovelli, whose pioneering works on the records of the Friuli 1976 and Irpinia 1980 earthquakes opened many doors toward understanding of seismic ground motions in Italy. This study was developed within the RETURN (multi-Risk sciEnce for resilienT commUnities undeR a changiNg climate) Foundation project, and within the Contract Agreement between RSE S.p.A. (Research on the Energy System) and the Italian Ministry of Economic Development. Authors are grateful to Aybige Akinci and Arben Pitarka for their constructive remarks during the review of the paper.

Open access publishing facilitated by Politecnico di Milano, as part of the Wiley - CRUI-CARE agreement.

Funding

This study received funding from the European Union Next-GenerationEU (National Recovery and Resilience Plan—NRRP, Mission 4, Component 2, Investment 1.3—D.D. 1243 2/8/2022, PE0000005), within the RETURN Extended Partnership, and by the Research Fund for the Italian Electrical System under the Contract Agreement between RSE S.p.A. and the Ministry of Economic Development - General Directorate for the Electricity Market, Renewable Energy and Energy Efficiency, Nuclear Energy in compliance with the Decree of April 16th, 2018.

Conflicts of Interest

The authors declare no conflicts of interest.

Data Availability Statement

Data used for the set-up of the numerical model include a DEM file available at https://portal.opentopography.org/. The earthquake ground-motion records used in the study come from https://esm-db.eu/, while macroseismic intensities fields are available at https://emidius.mi.ingv.it/CPTI15-DBMI15/query_eq/. The SPEED code used in the computations is available at https://speed.mox.polimi.it/. On the same website, pre and post processing Matlab and Phyton tools are available in the https://speed.mox.polimi.it/download/ section (as Additional materials). Post processing evaluations of impulsive features used the Matlab algorithms available at https://github.com/shreyshahi/PulseClassification.

References

Akinci, A., A. Pitarka, P. Artale Harris, P. De Gori, and M. Buttinelli. 2024. "Impact of the Earthquake Rupture on Ground-Motion Variability of the 24 August 2016 Mw 6.2 Amatrice, Italy, Earthquake." *Bulletin of the Seismological Society of America* 114: 2823–2845.

Ameri, G., A. Emolo, F. Pacor, and F. Gallovic. 2011. "Ground-Motion Simulations for the 1980 M. 6.9 Irpinia Earthquake (Southern Italy) and Scenario Events." *Bulletin of the Seismological Society of America* 101: 1136–1151.

Artale Harris, P., A. Pitarka, A. Akinci, and A. Cuius. 2025. "Broadband Near-Fault Ground-Motion Simulations Using a Modified f-k Method in Central Italy." *Bulletin of the Seismological Society of America* 1: 22. https://doi.org/10.1785/0120250165.

Ascione, A., S. Nardò, and S. Mazzoli. 2020. "The MS, Irpinia Earthquake from the Basement to the Surface: A Review of Tectonic Geomorphology and Geophysical Constraints, and New Data on Post Seismic Deformation." *Geosciences* 10, no. 12: 493. https://doi.org/10.3390/geosciences10120493 1980.

Baltzopoulos, G., E. Chioccarelli, and I. Iervolino. 2015. "The Displacement Coefficient Method in Near-Source Conditions." *Earthquake Engineering & Structural Dynamics* 44: 1015–1033. https://doi.org/10.1002/eqe.2497.

Baltzopoulos, G., L. Luzi, and I. Iervolino. 2020. "Analysis of Near-Source Ground Motion from the 2019 Ridgecrest Earthquake Sequence." *Bulletin of the Seismological Society of America* 110: 1495–1505.

Bernard, P., and A. Zollo. 1989. "The Irpinia (Italy) 1980 Earthquake: Detailed Analysis of a Complex Normal Faulting." *Journal of Geophysical Research* 94: 1631–1648. https://doi.org/10.1029/JB094iB02p01631.

Bolt, B. 2010. "Engineering Seismology", Earthquake Engineering: From Engineering Seismology to Performance-Based Engineering. Ch. 2. Edited by Y. Bozorgnia, and V. V. Bertero. CRC Press.

Bortolotti, T., R. Peli, G. Lanzano, S. Sgobba, and A. Menafoglio. 2024. "Weighted Functional Data Analysis for the Calibration of a Ground Motion Model in Italy." *Journal of the American Statistical Association* 119, no. 547: 1697–1708. https://doi.org/10.1080/01621459.2023.2300506.

Cauzzi, C., D. Fäh, V. Pessina, E. Faccioli, and C. Smerzini. 2012. Topographic Amplification from Recorded ear*th*quake Data and Numerical Simulations. (WCEE).

CEN. 2004. "Eurocode 8 Design of Structures for Earthquake Resistance -Part 1: General Rules, Seismic Actions and Rules for Buildings," (European Committee for Standardization).

Chiocchiarelli, E., and I. Iervolino. 2010. "Near-Source Seismic Demand and Pulse-Like Records: A Discussion for L'Aquila Earthquake." *Earthquake Engineering & Structural Dynamics* 39, no. 9: 1039–1062.

Cocco, M., and F. Pacor. 1993. "The Rupture Process of the 1980 Irpinia, Italy, Earthquake from the Inversion of Strong Motion Waveforms." *Tectonophysics* 218: 157–177.

Convertito, V., and N. A. Pino. 2014. "Discriminating among Distinct Source Models of the 1908 Messina Straits Earthquake by Modelling Intensity Data through Full Wavefield Seismograms." *Geophysical Journal International* 198: 164–173. https://doi.org/10.1093/gji/ggu128.

Cotecchia, V., A. Salvemini, and N. A. Ventrella. 1990. "Interpretazione Degli Abbassamenti Territoriali Indotti Dal Terremoto del 23 Novembre 1980 e Correlazioni Con i Danni Osservati Su Talune Strutture Ingegneristiche Dell'area Epicentrale Irpina." *Rivista Italiana di Geotecnica* 4: 145–158.

Dello Russo, A., S. Sica, S. Del Gaudio, R. De Matteis, and A. Zollo. 2017. "Near-Source Effects on the Ground Motion Occurred at the Conza Dam Site (Italy) during the 1980 Irpinia Earthquake." *Bulletin of Earthquake Engineering* 15: 4009–4037. https://doi.org/10.1007/s10518-017-0138-2.

DISS Working Group. 2025. "Database of Individual Seismogenic Sources (DISS), Version 3.3.1: A Compilation of Potential Sources for Earthquakes Larger than M. 5.5 in Italy and Surrounding Areas." *Istituto Nazionale Di Geofisica e Vulcanologia (INGV)*, https://doi.org/10.13127/diss3.3.1.

Dreger, D., G. Hurtado, A. Chopra, and S. Larsen. 2011. "Near-Field Across-Fault Seismic Ground Motions." *Bulletin of the Seismological Society of America* 101, no. 1: 202–221.

Evangelista, L., S. del Gaudio, C. Smerzini, et al. 2017. "Physics-Based Seismic Input for Engineering Applications: A Case Study in the Aterno River Valley, Central Italy." *Bulletin of Earthquake Engineering* 15: 2645–2671.

Faccioli, E., R. Paolucci, and J. Rey. 2004. "Displacement Spectra for Long Periods." *Earthquake Spectra* 20: 347–376.

Gomez-Capera, A. A., M. D'Amico, G. Lanzano, et al. 2020. "Relationships between Ground Motion Parameters and Macroseismic Intensity for Italy." *Bulletin of Earthquake Engineering* 18: 5143–5164. https://doi.org/10.1007/s10518-020-00905-0.

Graves, R. W., T. H. Jordan, S. Callaghan, et al. 2011. "CyberShake: A Physics-Based Seismic Hazard Model for Southern California." *Pure and Applied Geophysics* 168: 367–381.

Graves, R., and A. Pitarka. 2016. "Kinematic Ground-Motion Simulations on Rough Faults Including Effects of 3D Stochastic Velocity Perturbations." *Bulletin of the Seismological Society of America* 106, no. 5: 2136–2153. https://doi.org/10.1785/0120160088.

Hisada, Y., and J. Bielak. 2003. "A Theoretical Method for Computing Near-Fault Ground Motions in Layered Half-Spaces Considering Static Offset Due to Surface Faulting, with a Physical Interpretation of Fling Step and Rupture Directivity." *Bulletin of the Seismological Society of America* 93: 1154–1168.

Iervolino, I., E. Chioccarelli, and G. Baltzopoulos. 2012. "Inelastic Displacement Ratio of Near-Source Pulse-Like Ground Motions." *Earthquake Engineering & Structural Dynamics* 41: 2351–2357.

Improta, L., M. Bonagura, P. Capuano, and G. Iannaccone. 2003. "An Integrated Geophysical Investigation of the Upper Crust in the Epicentral Area of the 1980, Ms=6.9, Irpinia Earthquake (Southern Italy." *Tectonophysics* 361: 1–169. https://doi.org/10.1016/S0040-1951(02)00588-7.

Infantino, M., I. Mazzieri, A. G. Ozcebe, R. Paolucci, and M. Stupazzini. 2020. "3D Physics-Based Numerical Simulations of Ground Motion in Istanbul from Earthquakes along the Marmara Segment of the North Anatolian Fault." *Bulletin of the Seismological Society of America* 110: 2559–2576.

Kamai, R., N. Abrahamson, and R. Graves. 2014. "Adding Fling Effects to Processed Ground-Motion Time Histories." *Bulletin of the Seismological Society of America* 104: 1914–1929.

Kenawy, M., D. McCallen, and A. Pitarka. 2021. "Variability of Near-Fault Seismic Risk to Reinforced Concrete Buildings Based on High-Resolution Physics-Based Ground Motion Simulations." *Earthquake Engineering & Structural Dynamics* 50: 1713–1733. https://doi.org/10.1002/eqe.3413.

Kohrangi, M., P. Bazzurro, D. Vamvatsikos, and A. Spillatura. 2017. "Conditional Spectrum-Based Ground Motion Record Selection Using Average Spectral Acceleration." *Earthquake Engineering & Structural Dynamics* 46: 1667–1685.

Lancieri, M., and A. Zollo. 2009. "Simulated Shaking Maps for the 1980 Irpinia Earthquake, Ms 6.9: Insightson the Observed Damage Distribution." *Soil Dynamics and Earthquake Engineering* 29: 1208–1219.

Lanzano, G., L. Luzi, F. Pacor, et al. 2019. "A Revised Ground Motion Prediction Model for Shallow Crustal Earthquakes in Italy." *Bulletin of the Seismological Society of America* 109: 525–540.

Lanzano, G., S. Sgobba, L. Caramenti, and A. Menafoglio. 2021. "Ground-Motion Model for Crustal Events in Italy by Applying the Multisource Geographically Weighted Regression (MS-GWR) Method." *Bulletin of the Seismological Society of America* 111, no. 6: 3297–3313. https://doi.org/10.1785/0120210044.

Lavrentiadis, G., N. A. Abrahamson, K. M. Nicolas, et al. 2023. "Overview and Introduction to Development of Non-Ergodic Earthquake Ground-Motion Models." *Bulletin of Earthquake Engineering* 21: 5121–5150. https://doi.org/10.1007/s10518-022-01485-x.

Locati, M., R. Camassi, A. Rovida, et al. 2022. "Database Macrosismico Italiano (DBMI15), versione 4.0. Istituto Nazionale di Geofisica e Vulcanologia (INGV)." https://doi.org/10.13127/dbmi/dbmi15.4.

Luzi, L., F. Pacor, R. Puglia, et al. 2017. "The Central Italy Seismic Sequence between August and December 2016: Analysis of Strong-Motion Observations." *Seismological Research Letters* 88, no. 5: 1–1231. https://doi.org/10.1785/0220170037.

Luzi, L., G. Lanzano, C. Felicetta, et al. 2020. "Engineering Strong Motion Database (ESM) (Version 2.0). Istituto Nazionale di Geofisica e Vulcanologia (INGV)." https://doi.org/10.13127/ESM.2.

Mavroeidis, G. P., and A. S. Papageorgiou. 2010. "Effect of Fault Rupture Characteristics on Near-Fault Strong Ground Motions." *Bulletin of the Seismological Society of America* 100, no. 1: 37–58. https://doi.org/10.1785/0120090018.

Mazzieri, I., M. Stupazzini, R. Guidotti, and C. Smerzini. 2013. "SPEED: SPectral Elements in Elastodynamics with Discontinuous Galerkin: A Non-Conforming Approach for 3D Multi-Scale Problems." *International Journal for Numerical Methods in Engineering* 95, no. 12: 991–1010.

McCallen, D. M., A. Petersson, A. Rodgers, et al. 2021. "EQSIM—A Multidisciplinary Framework for Fault-to-Structure Earthquake Simulations on Exascale Computers Part I: Computational Models and Workflow." *Earthquake Spectra* 37, no. 2: 707–735.

Miah, M., D. McCallen, A. Pitarka, and F. Petrone. 2024. "Simulation-Based Characterization of the Variability of Earthquake Risk to Buildings in the Near-Field." *Earthquake Engineering & Structural Dynamics* 53: 237–260. https://doi.org/10.1002/eqe.4007.

Monsalvo-Franco, E. I., C. Smerzini, A. Rosti, M. Rota, A. Penna, and R. Paolucci. 2025. "Seismic Fragility Curves with Unconventional Ground Motion Intensity Measures from Physics-Based Simulations." *Bulletin of Earthquake Engineering* 23, no. 5: 1885–1915.

Munafò, I., A. Akinci, M. Taroni, et al. 2024. "Studying Past Earthquakes with Modern Techniques: Ground Motion Simulations for the 11 January 1693 Noto Earthquake in Italy." *Seismological Research Letters* 95: 3387–3405.

O'Connel, D. R. H., S. Ma, and R. J. Archuleta. 2007. "Influence of Dip and Velocity Heterogeneity on Reverse- and Normal-Faulting Rupture Dynamics and Near-Fault Ground Motions." *Bulletin of the Seismological Society of America* 97, no. 6: 1970–1989.

Pantosti, D., and G. Valensise. 1993. "Source Geometry and Long-Term Behaviour of the 1980, Irpinia Earthquake Fault Based on Field Geologic Observations." *Annals of Geophysics* 36, no. 1.

Paolucci, R., C. Smerzini, and M. Vanini. 2021. "BB-SPEEDset: A Validated Dataset of Broadband Near-Source Earthquake Ground Motions from 3D Physics-Based Numerical Simulations." *Bulletin of the Seismological Society of America* 111, no. 5: 2527–2545. https://doi.org/10.1785/0120210089.

Paolucci, R., F. Gatti, M. Infantino, and C. Smerzini. 2018b. "AG Özcebe, and M Stupazzini 2018b. Broadband Ground Motions from 3D Physics-Based Numerical Simulations Using Artificial Neural Networks." *Bulletin of the Seismological Society of America* 108: 1272–1286.

Paolucci, R., I. Mazzieri, and C. Smerzini. 2015. "Anatomy of Strong Ground Motion: Near-Source Records and Three-Dimensional Physics-Based Numerical Simulations of the Mw 6.0 2012 May 29 Po Plain Earthquake." *Geophysical Journal International* 203, no. 3: 2001–2020.

Paolucci, R., L. Evangelista, I. Mazzieri, and E. Schiappapietra. 2016. "The 3D Numerical Simulation of Near-Source Ground Motion during the Marsica Earthquake, Central Italy, 100 Years Later." *Soil Dynamics and Earthquake Engineering* 91: 39–52. https://doi.org/10.1016/j.soildyn.2016.09.023.

Paolucci, R., M. Infantino, I. Mazzieri, A. G. Özcebe, C. Smerzini, and M. Stupazzini. 2018a. "3D Physics-Based Numerical Simulations: Advantages and Current Limitations of a New Frontier to Earthquake Ground Motion Prediction. The Istanbul Case Study," In Recent Advances in Earthquake Engineering in Europe (K. Pitilakis ed.), Geotechnical, *Geological and Earthquake Engineering Series*. (Springer, 203–223).

Pitarka, A., A. Akinci, P. De Gori, and M. Buttinelli. 2022. "Deterministic 3D Ground-Motion Simulations (0-5 Hz) and Surface Topography Effects of the 30 October 2016 Mw 6.5 Norcia, Italy, Earthquake." *The Bulletin of the Seismological Society of America* 112: 262–286.

Porfido, S., E. Esposito, L. Guerrieri, E. Vittori, G. Tranfaglia, and R. Pece. 2007. "Seismically Induced Ground Effects of the 1805, 1930 and 1980 Earthquakes in the Southern Apennines, Italy." *Italian Journal of Geosciences* 126: 333–346.

Porfido, S., G. Alessio, G. Gaudiosi, R. Nappi, and A. M. Michetti. 2022. "40 Years Later: New Perspectives on the 23 November 1980, Ms 6.9, Irpinia-Lucania Earthquake," *Geosciences* 12: 173. https://doi.org/10.3390/geosciences12040173.

Postpischl, D., A. Branno, E. Esposito, et al. 1985. "The Irpinia Earthquake of November 23, 1980," In Atlas of Isoseismal Maps of Italian Earthquakes. D. Postpischl, (CNR-PFG).

Rosti, A., C. Smerzini, R. Paolucci, A. Penna, and M. Rota. 2023. "Validation of Physics-Based Ground Shaking Scenarios for Empirical Fragility Studies: The Case of the 2009 L'Aquila Earthquake." *Bulletin of Earthquake Engineering* 21: 95–123.

Rovelli, A. 1983. "Frequency Relationship for Seismic Qβ of Central-Southern Italy from Accelerograms for the Irpinia Earthquake (1980)." *Physics of the Earth and Planetary Interior* 32: 209–217.

Rovida, A., M. Locati, R. Camassi, B. Lolli, P. Gasperini, and A. Antonucci. 2022. "Italian Parametric Earthquake Catalogue (CPTI15), version 4.0. INGV." https://doi.org/10.13127/cpti/cpti15.4.

Sgobba, S., C. Felicetta, G. Lanzano, F. Ramadan, M. D'Amico, and F. Pacor. 2021a. "NESS2.0: An Updated Version of the Worldwide Dataset for Calibrating and Adjusting Ground-Motion Models in Near Source." *Bulletin of the Seismological Society of America* 111: 2358–2378.

Sgobba, S., G. Lanzano, and F. Pacor. 2021c. "Empirical Nonergodic Shaking Scenarios Based on Spatial Correlation Models: An Application to Central Italy." *Earthquake Engineering & Structural Dynamics* 50: 60–80. https://doi.org/10.1002/eqe.3362.

Sgobba, S., G. Lanzano, F. Pacor, and C. Felicetta. 2021b. "An Empirical Model to Account for Spectral Amplification of Pulse-Like Ground Motion Records." *Geosciences* 11, no. 1: 15. https://doi.org/10.3390/geosciences11010015.

Shahi, S. K., and J. W. Baker. 2014. "An Efficient Algorithm to Identify Strong-Velocity Pulses in Multicomponent Ground Motions." *Bulletin of the Seismological Society of America* 104: 2456–2466.

Smerzini C., and Villani, M. 2012. "Broadband Numerical Simulations in Complex Near Field Geological Configurations: the Case of the M_w 6.3 2009 L' Aquila Earthquake." *Physics of the Earth and Planetary Interiors* 102: 2436–2451.

Smerzini, C., C. Amendola, R. Paolucci, and A. Bazrafshan. 2024. "Engineering Validation of BB-SPEEDset, a Data Set of Near-Source Physics-Based Simulated Accelerograms." *Earthquake Spectra* 40: 420–445.

Smerzini, C., M. Vanini, R. Paolucci, P. Renault, and P. Traversa. 2023. "Regional Physics-Based Simulation of Ground Motion Within the Rh-ne Valley, France, during the M_W 4.9 2019 Le Teil Earthquake." *Bulletin of Earthquake Engineering* 21: 1747–1774.

Somerville, P. G. 2003. "Magnitude Scaling of the Near Fault Rupture Directivity Pulse." *Physics of the Earth and Planetary Interiors* 137, no. 1–4: 201–212.

Somerville, P. G., N. F. Smith, R. W. Graves, and N. A. Abrahamson. 1997. "Modification of Empirical Strong Ground Motion Attenuation Relations to Include the Amplitude and Duration Effects of Rupture Directivity." *Seismological Research Letters* 68, no. 1: 199–222.

Stupazzini, M., M. Infantino, A. Allmann, and R. Paolucci. 2021. "Physics-Based Probabilistic Seismic Hazard and Loss Assessment in Large Urban Areas: A Simplified Application to Istanbul." *Earthquake Engineering & Structural Dynamics* 50, no. 1: 99–115.

Stupazzini, M., R. Paolucci, and H. Igel. 2009. "Near-Fault Earthquake Ground-Motion Simulation in the Grenoble Valley by a High-Performance Spectral Element Code." *Bulletin of the Seismological Society of America* 99: 286–301.

Tinti, E., L. Scognamiglio, A. Cirella, and M. Cocco. 2014. "Up-Dip Directivity in Near-Source during the 2009 L'Aquila Mainshock." *Geophysical Journal International* 198: 1618–1631.

Westaway, R. 1993. "Fault Rupture Geometry for the 1980 Irpinia Earthquake: A Working Hypothesis." *Annals of Geophysics* 36: 51–70.

Yen, M. H., S. von Specht, Y. Y. Lin, F. Cotton, and K. F. Ma. 2021. "Within- and Between-Event Variabilities of Strong-Velocity Pulses of Moderate Earthquakes Within Dense Seismic Arrays." *Bulletin of the Seismological Society of America* 112: 361–380.

Zollo, A, A. Orefice, V. Convertito. 2014. "Source Parameter Scaling and Radiation Efficiency of Microearthquakes Along the Irpinia Fault Zone in Southern Apennines, Italy". *Journal of Geophysical Research: Solid Earth* 119: 3256–3275. https://doi.org/10.1002/2013JB010116.